

LASER RADIATION SCATTERING

PACS numbers: 42.25.Fx; 47.55.dd
DOI: 10.1070/QE2009v039n04ABEH013892

Determination of the microstructure of gas bubbles in highly purified water by measuring the elements of the laser radiation scattering matrix

N.F. Bunkin, N.F. Suyazov, A.V. Shkirin, P.S. Ignat'ev, K.V. Indukaev

Abstract. **Modulation interference microscopy and measurements of the elements of the light scattering matrix showed that doubly distilled water purified from solid impurities contains macroscopic scatterers in the form of micron clusters formed by polydisperse air bubbles with the effective radius 70 – 90 nm. The fractal dimension of clusters lies within 2.4 – 2.8 and their concentration is $\sim 10^6$ cm^{-3}.**

Keywords: *scattering matrix, fractal clusters.*

1. Introduction: Formulation of the problem

The measurement of the indicatrix of scattered laser radiation in a goniometric scheme is known to be the most efficient method for studying the structure, size and distribution of scattering objects [1 – 7]. In the last 10 – 15 years, methods based on the measurement of polarisation parameters of radiation, namely, the angular dependences of the scattering matrix elements are gaining in importance. In this case, we are dealing with the Mueller matrix (see [1 – 3, 8] and references therein). These methods are widely used in the studies of the composition of cosmic dust [4] and volcanic ash [5], the structure of aerosols formed by ice microcrystals and water drops [6, 7], etc. These papers show that the measurement of the angular dependences of the Mueller matrix coefficients give sufficiently accurate information on the size distribution of scattering particles. If the size of these particles exceeds the laser radiation wavelength (Mie particles), by measuring different elements of the Mueller matrix, it is possible to find whether these particles are 'monolithic' or they consist of individual monomers of size smaller than the radiation wavelength (i.e. Rayleigh particles) [9 – 11]. Moreover, these methods allow the determination of the type of monomer aggregation resulting in the formation of Mie particles [10].

The latter circumstance is very important in the context of the problem formulated below. As shown in a number of papers, any liquid, saturated with dissolved gas (for example, atmospheric air) and containing an ionic component, is unstable with respect to the spontaneous formation of spherical nanometre cavities – bubstons (bubbles stabilised by ions) [12, 13]. Bubstons are stable gas nanobubbles, whose stability is caused by adsorption of ions of the same sign on their surface. Coulomb repulsion forces produced in this case and acting along the bubston surface compensate for surface tension forces, providing thereby the mechanical equilibrium of the bubston. The radii of bubstons in aqueous solutions of an electrolyte with the ion concentration of $10^{15} - 10^{16}$ cm^{-3} (i.e. in diluted solutions) are 10 – 100 nm. It was shown in [12, 13] that, when the mechanical equilibrium is achieved, the gas pressure inside an individual bubston is equal to that over the liquid surface. This provides the diffusion stability of the bubston with respect the gas dissolved in liquid. Finally, the problem of the Coulomb screening of a charge bubston in the aqueous electrolyte solution was solved in [13], where the action of viscous friction forces on the charge bubston surrounded by a cloud of counter-ions was also considered. The viscous friction efficiently 'washes away' peripheral layers in the counter-ion cloud, and two types of composite particles appear in the equilibrium state. They represent charged gas nuclei surrounded by a cloud of counter-ions of different (but fixed) thickness. It is shown that these composite particles are not electrically neutral but have opposite electric charges. Because of this, they coagulated with each other in the attracting Coulomb field to form bubston clusters. According to the model developed in [13], a bubston cluster has the characteristic radius ~ 0.5 μm and contains $\sim 10^2 - 10^3$ individual bubstons. Note that the stabilisation of the bubble due to the charging of its surface is an alternative to the mechanism of mechanical and diffusion stabilisation based on the embedding gas molecules into pores and cracks in solid particles [14, 15].

In this paper, we confirm experimentally the existence of bubston clusters in water purified from external solid impurities. Experiments were performed in two stages. At the first stage, water samples containing an ionic component (the specific resistance was 2 MΩ cm, which were highly purified from solid microscopic impurities, were studied by using a modulation interference microscope. The known suspensions of colloidal silica and polystyrene latex dissolved in the same water were also studied. Note that the microscope that we used gives not only the size of particles dissolved in water but also their optical quality. We found in experiments that water purified from external impurities does contain micron particles, the optical density related to

N.F. Bunkin, N.F. Suyazov, A.V. Shkirin Wave Research Center, A.M. Prokhorov General Physics Institute, Russian Academy of Sciences, ul. Vavilova 38, 119991 Moscow, Russia;
e-mail: nbunkin@kapella.gpi.ru;
P.S. Ignat'ev, K.V. Indukaev Amphora Laboratories, Limited Liability Company, ul. 5-ya Magistral'naya 11, office 18, 123007 Moscow, Russia

Received 29 April 2008; revision received 3 October 2008
Kvantovaya Elektronika **39** (4) 367 – 381 (2009)
Translated by M.N. Sapozhnikov

them being lower than the optical density of water. At the second stage, we investigated the angular dependences of the elements of the Mueller matrix for the same water samples and suspensions of colloidal silica and latex. In addition, we proved that micron particles, contained in water purified from external impurities, consist in turn of monomers of nanometre size.

Note that our study develops earlier works [16–18] in this field at a qualitatively new level. In this paper, we do not consider any theoretical models describing the nucleation of bubstons, their stabilisation due to specific adsorption of ions on their surface, and their diffusion-controlled coagulation accompanied by the formation of bubston clusters. In our opinion, the corresponding theory should be published elsewhere.

2. Modulation interference laser microscopy experiment

A MIM-3 microscope (Amphora Laboratories Limited Liability Company) is described in detail in [18, 19]. This is a two-channel microscope, in which one measurement channel is a classical white light microscope, while the second channel is a high-resolution laser interferometer operating at a wavelength of 532 nm. The laser radiation intensity focused on a sample by a microobjective with a set of apertures (see below) is ~ 1 W cm^{-2}, which, taking into account low absorption (the absorption coefficient of distilled water at this wavelength is $\sim 10^{-4}$ cm^{-1}), allows us to neglect the heating of samples. By using the image of a sample in white light (the field of view in this channel is 100 times larger than that in the interference channel), we can select a fragment of a sample of interest to study it by the method of coherent phase microscopy.

The interference channel of the microscope is shown schematically in Fig. 1. The scheme of this channel coincides, accurate to the use of microobjectives, with that of a Mach–Zehnder interferometer. A distinct feature of our microscope is the use of a phase modulator in the reference arm. A cell with liquid is mounted on a movable stage under microobjective O1. A collimated laser beam passes through a $\lambda/2$ plate and is split in beamsplitter PBS with a polarisation coating. Elements C1 and C2, which consist of quarter- and half-wave phase plates, are used to correct radiation polarisation in both channels. By changing the tilt of the $\lambda/2$ plate, we can vary the energy distribution between two beams behind the beamsplitter to provide the optimal contrast of an interferogram irrespective of a jump in the optical density of the object with respect to the optical density of the environment.

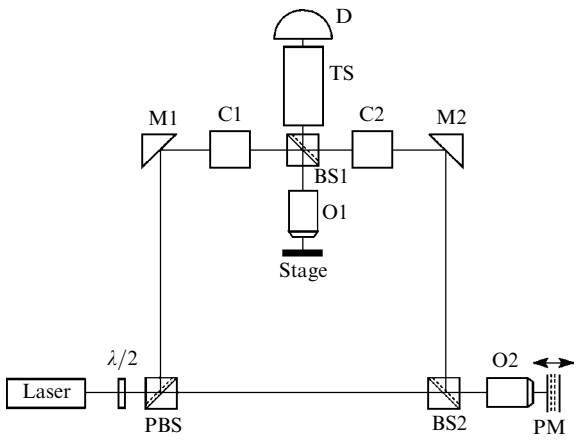

Figure 1. Scheme of the interference channel of a MIM-3 microscope.

One of the two beams behind the beamsplitter (object beam) is reflected from mirror M1 and is split again in beamsplitter BS1. The reflected part of the beam is incident on microobjective O1 and illuminates a cell with liquid. This allows us to investigate the distribution of the phase difference of the object and reference beams along a selected plane in the liquid volume. The position of this plane along the liquid layer height is controlled by adjusting microobjective O1. The light propagated through an object in the liquid and reflected by a mirror substrate of the cell (the cell design is described below) is collected by the same objective O1; then, the light propagates through beamsplitter BS1 and telescopic system TS and is incident on a CMOS array D. Note that the use of microobjective O1 imposes certain restrictions of the liquid layer thickness because this microobjective tightly focuses beams illuminating the object under study. These beams diverge behind the focal plane, reflect from the mirror substrate and fall again on the same microobjective O1. As will be shown below, an interferogram is obtained by using paraxial beams with a small angle of deviation from the optical axis upon focusing and subsequent reflection. These beams fall into microobjective O1 after reflection. It is clear, however, that, when the aperture of microobjective is fixed, the number of such beams increases with decreasing distance between the focus of microobjective O1 and the mirror substrate.

The reference beam passes through beamsplitter PBS and is incident on beamsplitter BS2. A part of the beam passes through microobjective O2, which is similar to microobjective O1. Near the focal plane of microobjective O2 a piezoelectric modulator PM is located, which consists of a plane mirror mounted on a piezoelectric element connected to a sinusoidal oscillation generator. The reference beam reflected from the piezoelectric modulator mirror passes again through microobjective O2 and falls on beamsplitter BS2, reflects from mirror M2 and falls on beamsplitter BS1, where it is mixed with the object beam, passes through telescopic system TS and falls on array D. A dynamic interference pattern produced on the array is processed with a personal computer.

The radiation intensity measured with array D in each pixel is described by the expression $I = I_1 + I_2 + 2(I_1 I_2)^{1/2} \times \cos\delta + I_n$, where I_1 and I_2 are the object and reference wave intensities, respectively; I_n is the background (incoherent) radiation intensity; and δ is the phase sift between the reference and object waves. It is this latter parameter that is of interest to us. The value of δ was determined by measuring the radiation intensity successively for each of the pixels of array D for four fixed phase shifts Δ_i ($i = 1, 2, 3, 4$) caused by the change in the arm length in the reference channel produced with the help of a phase modulator. For each of the pixels, the system of four equations

$$I(1) = I_1 + I_2 + 2(I_1 I_2)^{1/2} \cos(\delta + \Delta_1) + I_n,$$

$$I(2) = I_1 + I_2 + 2(I_1 I_2)^{1/2} \cos(\delta + \Delta_2) + I_n,$$

$$I(3) = I_1 + I_2 + 2(I_1 I_2)^{1/2} \cos(\delta + \Delta_3) + I_n,$$

$$I(4) = I_1 + I_2 + 2(I_1 I_2)^{1/2} \cos(\delta + \Delta_4) + I_n$$

was solved. By measuring the value of δ for each pixel of the array, we obtain in fact the optical density distribution in the array plane. Note that the interference of the reference and object waves is best realised for paraxial beams (in this case, the contribution I_n of the incoherent background will be suppressed). For this reason, a region of array D is selected (the area of this region is considerably smaller than the array area) on which paraxial beams are incident, and the interference pattern is recorded for this region. The part of the object, which can be processed in such a way, is determined by the magnification of microobjective O1, being nevertheless only a small part of the object under study. By moving the stage in a plane perpendicular to the optical axis with a step determined by the area of the selected region and recording interferograms at each step, we can obtain the optical density distribution along the object with the specified accuracy.

The cell with liquid is schematically shown in Fig. 2. A liquid drop was placed on the surface of a polished plane aluminium mirror on which a transparent Al_2O_3 layer was deposited. On the surface of this layer gold electrodes were deposited to which a dc voltage up to 500 V was applied for determining the sign of the electric charge of particles in liquid. The liquid layer thickness was fixed by means of 10-μm-thick semicircular C-shaped Teflon spacers. A 0.17-mm-thick cover glass was pressed from above to these spacers by means of a circular C-clamp. All the cover glasses were used only one time. The surfaces of the mirror and cover glass were degreased before each measurement, first with ethylene and then with toluene. Note that neither hydrophobic nor hydrophilic properties were imparted initially to surfaces contacting with water. Note also that, when the liquid was poured into the cell, special attention was paid to provide the absence of air 'islands' in the filled cell: the entire cell volume limited by the Teflon spacer should be uniformly filled; at the same time, liquid was in contact with the atmospheric air at the gap of the Teflon spacer. The area of the liquid layer in the cell was ~ 1 cm^2, while the depth of focus of microobjective O1 was ~ 2 μm, i.e. it was considerably smaller than the liquid film thickness. This provided the high-contrast white-light images of particles inside the liquid layer directly adjacent to the cover glass and also allowed the image scan over the liquid depth.

The setup was calibrated by using reflection Michelson etalons with steps of different heights (the minimal step height was 5 nm) and also monodisperse spherical colloidal silica particles with radii 0.43, 0.8, and 2.6 μm. We studied samples of twice distilled water purified from solid microimpurities with the help of a porous membrane FiTremM 1 filter with an average pore radius of 100 nm and suspensions of colloidal silica particles of radius 0.8 μm and polystyrene latex particles of radius 200 nm in the same water. As mentioned above, the specific resistance of the water samples was 2 MΩ cm, i.e. these samples were not deionised.

A white-light microscopic photograph (Fig. 3a) shows colloidal silica particles of radius 0.8 μm in pure water after their sedimentation on a cell bottom. The mutual arrangement of this particles is random rather than ordered, and particles themselves tend to coagulate. Figure 3b presents the optical density distribution measured in the vicinity of a silica particle. On the vertical axis the optical path difference (path shift) is plotted in the units of $\lambda\delta$, where λ is the wavelength. Thus, the phase shift is measured conventionally in nanometres (taking into account the instrumental

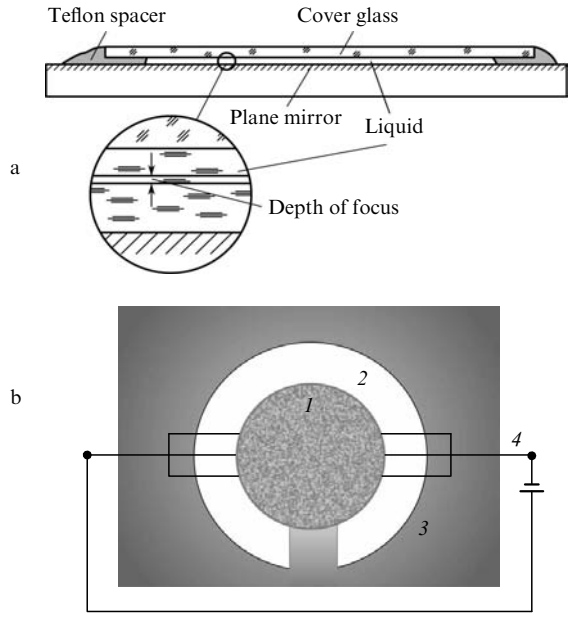

Figure 2. Scheme of a cell with liquid: the front (a) and top (b) views: (*1*) liquid layer; (*2*) Teflon spacer; (*3*) aluminum substrate; (*4*) electrodes.

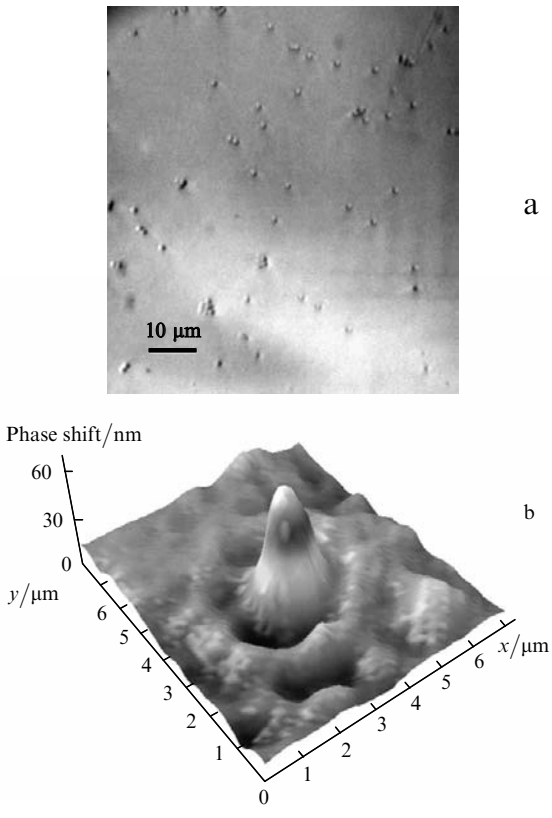

Figure 3. Photograph of colloidal silica particles in the white light of a microscope (a) and the phase shift distribution on a colloidal silica particle (b).

function of the setup measured for spherical particles), while horizontal axes xy specify a plane in which a particle is located. In fact, we can determine from them the size of particles under study. One can see that the positive phase shift corresponds to particles with a higher optical density (the refractive indices n of fused silica and water at a wavelength of 532 nm are 1.46 and 1.33, respectively).

Figure 4 presents the optical density distribution (phase shift) in the vicinity of a latex particle of radius 0.2 μm; note that we failed to obtain high-qiality photographs for latex particles in white light. As it should be, the optical density of this particle (polystyrene, $n = 1.59$) is higher than that of water.

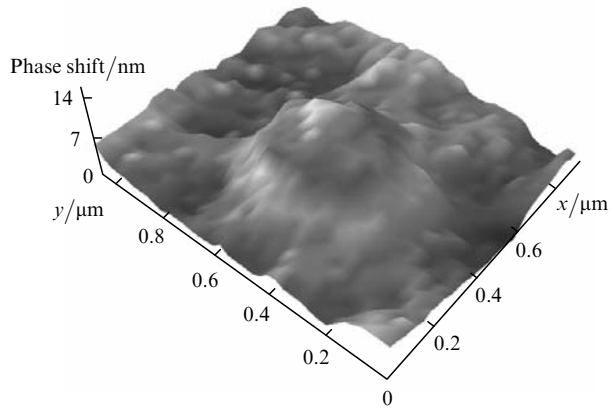

Figure 4. Phase shift distribution on a polystyrene latex particle.

Figure 5a presents a white-light photograph of the liquid layer-atmosphere interface for pure water at the gap of the C-spacer. A region of the water–air interface (broad black band) in this figure separates air at the bottom from water at the top. The phase shift distribution across the interface is presented in Fig. 5b. One can see that the jump of the optical density occurs at the interface, and the phase shift decreases in the gas phase. The thickness of the boundary layer of the liquid inside which its optical density drastically decreases is determined from coordinates in the xy plane in the figure.

Figure 6a shows a pure water layer far from the interface. A macroscopic particle of size ~ 1 μm located near the cover glass surface is clearly seen. Figure 6b presents the optical density distribution for this particle. One can see that this particle has a lower optical density than that of the surrounding water (as in the case of the water–air interface, the phase incursion in this particle is negative). This particle can be only a gas bubble (or a bubston cluster) because a random penetration of environmental particles with a lower optical density into the cell was excluded by special dust removal of the laboratory setup. Because the liquid under study was not preliminarily degassed, gas bubbles contained dissolved air.

We constructed histograms over r for colloidal silica and latex particles and particles with a low optical density found

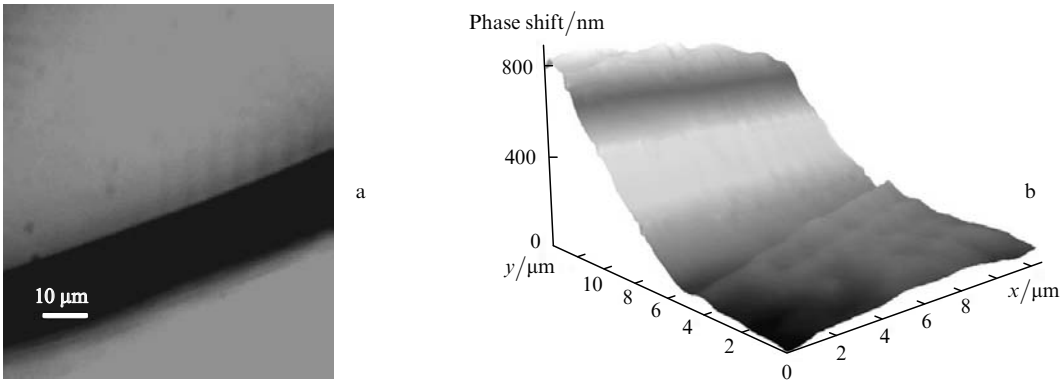

Figure 5. Photography of the liquid–air interface in the gap of a Teflon spacer (a) and the phase shift distribution across this boundary (b).

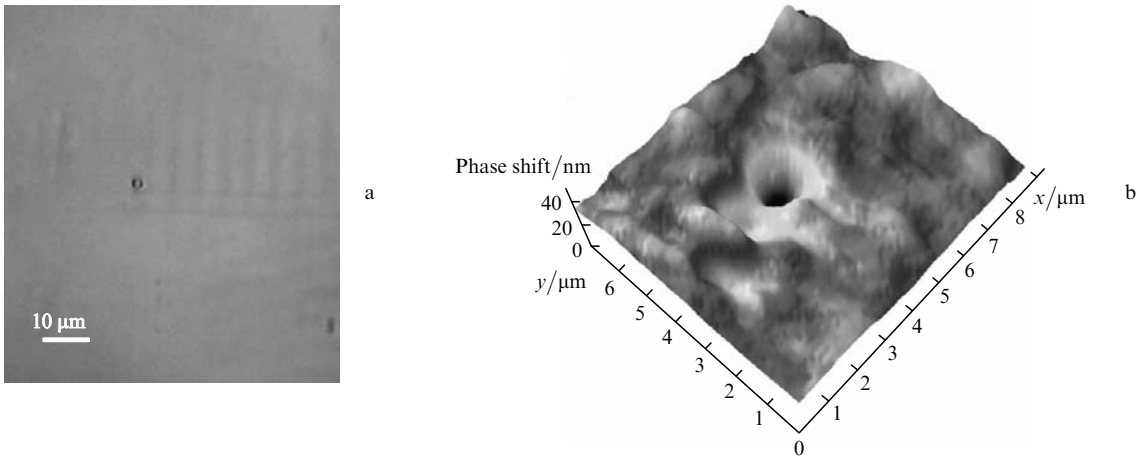

Figure 6. Photography of a macroscopic particle of a low optical density in the white light of a microscope (a) and the phase shift distribution on a macroscopic particle of a low optical density (b).

in water, which then were approximated by the logarithmically normal distribution. The corresponding distributions with calculated parameters are

$$r_{\text{eff}} = \frac{\int_0^\infty \rho(r) r^3 \mathrm{d}r}{\int_0^\infty \rho(r) r^2 \mathrm{d}r},$$

$$\upsilon_{\text{eff}} = \frac{\int_0^\infty \rho(r)(r - r_{\text{eff}})^2 r^2 \mathrm{d}r}{r_{\text{eff}}^2 \int_0^\infty \rho(r) r^2 \mathrm{d}r},$$

where $\rho(r)$ is the probability density distribution (in our case, the logarithmically normal distribution), are presented in Fig. 7.

Particles with a low optical density retain their shape during the entire experiment (tens of minutes), i.e. they are in fact quasi-stable. If these particles are indeed micron air bubbles, at least two mechanisms of their quasi-stability can be proposed. The first mechanism is related to the generation of such bubbles on stable hydrophobic defects in the cover glass. The second mechanism assumes the simultaneous mechanical and diffusion equilibrium of the bubbles not only near the solid surface but also in the liquid volume. In this case, the gas pressure inside a bubble should be equal to that over the liquid surface, while surface tension forces should be compensated by some way. Such conditions are realised for bubstons and bubston clusters, the surface tension force being compensated due to the charging of a bubble surface by ions of the same sign. The latter is confirmed by many experiments in which an electrostatic field was applied to micron particles with the low optical density. It was found that these particles move towards a positive electrode, i.e. they were negatively charged. We did not attempt in these experiments to measure accurately the charge of particles (we are performing detailed measurements of the negative charge of particles at present). It was the presence of such a charge itself that was important for us. Note also the negative charge of particles is indirectly confirmed by their ability to move under the action of an electrostatic field. It is known (see, for example [20–23] that at the water–glass interface the dissociation of end groups occurs:

$$\mathrm{SiOH} \rightleftarrows \mathrm{SiO}^- + \mathrm{H}^+.$$

In this case, a positive H^+ ion in neutral water and alkali aqueous solution can pass to liquid, and the water–glass interface proves to be negatively charged. Thus, a negatively charged particle near the charged interface is subjected to the action of the Coulomb repulsion force directed downward, which is balanced by the Archimedean force directed upward, i.e. negatively charges particles near such an interface have neutral floatability and can move in the external Coulomb field. Note that the shape of these particles is not distorted near the boundary, which is important for the interpretation of results presented below.

Below, we describe experimental measurements of the angular dependences of the Mueller matrix. The results of these measurements in conjunction with the results presented above allow us to interpret unambiguously micron particles produced spontaneously in purified water as bubston clusters.

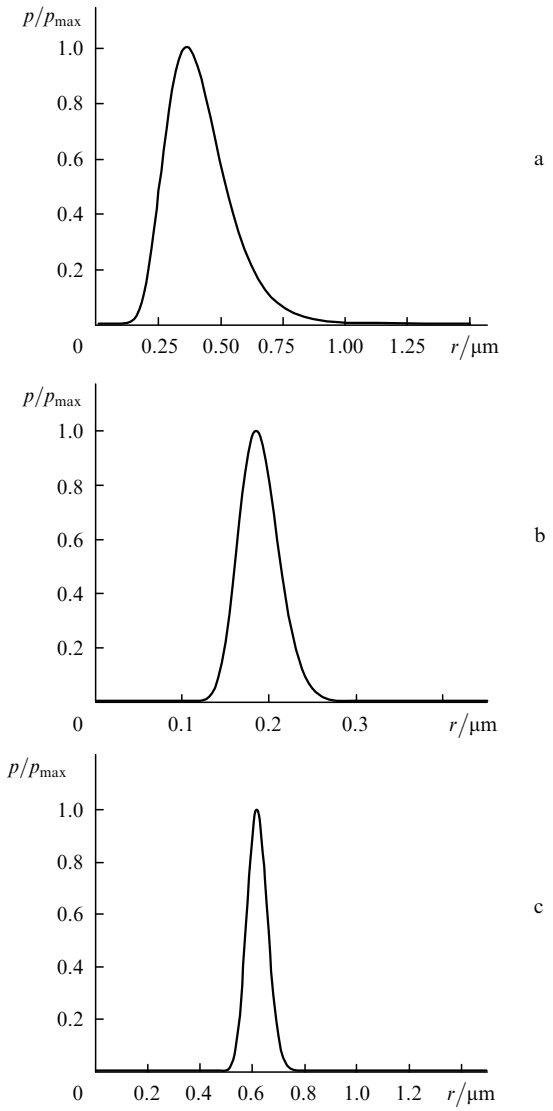

Figure 7. Logarithmically normal size distributions of macroscopic particles of a low optical density ($r_{\text{eff}} = 0.5$ μm, $\upsilon_{\text{eff}} = 0.1$) (a), polystyrene latex ($r_{\text{eff}} = 195$ nm, $\upsilon_{\text{eff}} = 0.015$) (b), and colloidal silica particles ($r_{\text{eff}} = 0.625$ μm, $\upsilon_{\text{eff}} = 0.004$) (c).

3. Measurement of the angular dependences of the Mueller matrix elements

3.1 Theoretical part

Consider a volume element of a scattering medium illuminated by a plane monochromatic wave with the wave vector k_{inc} directed along the z axis (Fig. 8). The direction of observation of a scattered wave is specified by the wave vector $\boldsymbol{k}_{\text{sca}}(\varphi, \theta)$. Because all the parameters of scatterers are distributed spatially uniformly, we will select as the scattering (observation) plane the xz plane corresponding to the azimuthal scattering angle $\varphi = 0$. In this case, the propagation direction of scattered radiation is unambiguously determined by the polar scattering angle θ. The amplitudes of incident and scattered waves are related by the expression [2]

$$\begin{pmatrix} E_{\parallel}^{(\text{sca})} \\ E_{\perp}^{(\text{sca})} \end{pmatrix} = \frac{\exp[\mathrm{i}k(R - z)]}{-\mathrm{i}kR} \begin{pmatrix} A_1 & A_2 \\ A_3 & A_4 \end{pmatrix} \begin{pmatrix} E_{\parallel}^{(\text{inc})} \\ E_{\perp}^{(\text{inc})} \end{pmatrix}, \qquad (1)$$

where A_1, A_2, A_3, and A_4 are elements forming the amplitude scattering matrix and depending on the scatter-

ing angle and orientation of particles with respect to the electromagnetic field strength vector of the incident wave; $k = 2\pi/\lambda$ is the wave number; λ is the radiation wavelength; R is the distance between a scatterer and a detector; and the absorption of radiation is neglected everywhere. The quantities $E_{\parallel}$ and $E_{\perp}$ are the perpendicular and parallel components of the electric field vector with respect to the observation plane. Because we measured the radiation intensity (the time-averaged square of the amplitude), it is necessary to know the relation between the intensities of the incident and scattered waves. The intensity and polarisation state of a light beam are completely described by the Stokes vector [1, 2, 8]:

$$\boldsymbol{S} = \begin{pmatrix} I \\ Q \\ U \\ V \end{pmatrix} = \begin{pmatrix} \langle E_{\parallel}E_{\parallel}^{*} + E_{\perp}E_{\perp}^{*}\rangle \\ \langle E_{\parallel}E_{\parallel}^{*} - E_{\perp}E_{\perp}^{*}\rangle \\ \langle E_{\parallel}E_{\perp}^{*} + E_{\parallel}^{*}E_{\perp}\rangle \\ \langle \mathrm{i}(E_{\parallel}E_{\perp}^{*} - E_{\parallel}^{*}E_{\perp})\rangle \end{pmatrix}, \tag{2}$$

where I is the total radiation intensity; Q is the difference of intensities of light waves polarised parallel and perpendicular to the plane of incidence of the wave; U is the difference of intensities of light waves propagated through linear polarisers and polarised at angles $+45^{\circ}$ and -45° with respect to the normal to the plane of incidence of the wave; V is the difference of intensities of circularly polarised waves with right- and left-hand polarisations. The interaction between the light wave and a scattering object can be described by the transformation of the Stokes vector $\boldsymbol{S}_{\mathrm{inc}}$ of the incident wave and the Stokes vector $\boldsymbol{S}_{\mathrm{sca}}$ of te scattered wave:

$$\boldsymbol{S}_{\mathrm{sca}} = [\boldsymbol{F}]\boldsymbol{S}_{\mathrm{inc}}, \tag{3}$$

or

$$\begin{pmatrix} I_{\mathrm{sca}} \\ Q_{\mathrm{sca}} \\ U_{\mathrm{sca}} \\ V_{\mathrm{sca}} \end{pmatrix} = \frac{1}{k^2R^2} \begin{pmatrix} F_{11} & F_{12} & F_{13} & F_{14} \\ F_{21} & F_{22} & F_{23} & F_{24} \\ F_{31} & F_{32} & F_{33} & F_{34} \\ F_{41} & F_{42} & F_{43} & F_{44} \end{pmatrix} \begin{pmatrix} I_{\mathrm{inc}} \\ Q_{\mathrm{inc}} \\ U_{\mathrm{inc}} \\ V_{\mathrm{inc}} \end{pmatrix}, \tag{4}$$

where [F] is the 4×4 Mueller matrix, or the scattering matrix.

The element $F_{11}(\theta)$ describes the scattering indicatrix of natural (randomly) polarised light, and the integrated quantity

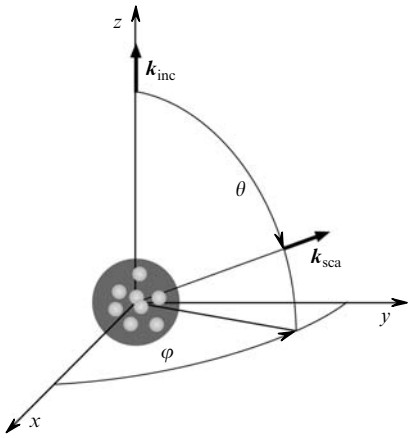

Figure 8. Geometry of the scattering experiment.

$$C_{\mathrm{sca}} = \frac{2\pi}{k^2}\int_0^{\pi} F_{11}(\theta)\sin\theta \mathrm{d}\theta \tag{5}$$

describes the total light scattering cross section. The Mueller matrix for randomly oriented scatterers with a symmetry plane has the block-diagonal form

$$[\boldsymbol{F}(\theta)] = \frac{1}{k^2R^2} \begin{pmatrix} F_{11} & F_{12} & 0 & 0 \\ F_{12} & F_{22} & 0 & 0 \\ 0 & 0 & F_{33} & F_{34} \\ 0 & 0 & -F_{34} & F_{44} \end{pmatrix}. \tag{6}$$

For particles small compared to the wavelength (Rayleigh particles), the Mueller matrix takes the form

$$[\boldsymbol{F}(\theta)] = \frac{B}{k^2R^2} \times \begin{pmatrix} \frac{1}{2}(1+\cos^2\theta) & \frac{1}{2}(\cos^2-1) & 0 & 0 \\ \frac{1}{2}(\cos^2\theta-1) & \frac{1}{2}(1+\cos^2\theta) & 0 & 0 \\ 0 & 0 & \cos\theta & 0 \\ 0 & 0 & 0 & \cos\theta \end{pmatrix}, \tag{7}$$

where

$$B = x^6\left|\frac{m^2-1}{m^2+1}\right|^2. \tag{8}$$

Here, $x = ka = 2\pi a/\lambda$ is the so-called size parameter; a is the radius of a spherical particle; and m is the complex refractive index of the particle with respect to the refractive index of the medium. Note that $x = 1$ for Rayleigh particles, and we will call particles for which this condition is not fulfilled the Mie scatterers.

More complex systems, such as clusters of spherical particles randomly distributed in size, orientation and aggregation type, are characterised by the scattering matrix having the approximately block-diagonal structure [9] with 'zero' matrix elements that are at least an order of magnitude smaller than the minimal nonzero matrix element. According to the numerical simulation of light scattering by clusters [9], the type of the dependence $F_{11}(\theta)$ is mainly determined by the size of monomers and their amount in a cluster.

3.2 Experimental part

We measured the elements of the scattering matrix for the same water samples as in experiments with the modulation interference microscope. The setup was calibrated by using suspensions of colloidal silica and polystyrene latex in this water (the colloidal silica suspension was studied at different silica concentrations). These concentrations were obtained by the aliquot dissolving of suspensions with the initial concentration n_{I}, which was determined with the help of a microscope by directly counting particles in a liquid layer with the fixed height and area. It was found that $n_{\mathrm{I}} \approx 2.1 \times 10^8$ cm^{-3} for colloidal silica particles, and the values of n_{I} measured for different samples are virtually the same. At the same time, the values of n_{I} for latex exhibited a large scatter from sample to sample, which is, probably, related to the general problem of visualisation of latex particles in water. First, these particles are poorly

discernible in the white light in the microscope (which is related to their size), i.e. they can be observed only by the methods of modulation interference microscopy. Second, the principal difference between colloidal silica and latex particles is that silica particles precipitate on the bottom of a cell (Fig. 2), where they remain at rest during the entire observation time, and therefore they amount can be easily determined. At the same time, smaller and less dense latex particles are, probably, distributed over the water layer height, and therefore to count them, it is necessary to scan the focus of objective O1 over height, i.e. to measure the height distribution of the optical density of the latex suspension. It is also necessary to take into account the diffusion of particles in liquid. In this case, one image of the type presented in Figs 3b, 4, 5b and 6b was obtained for a few seconds (which is related to the specificity of obtaining such an image and subsequent computer processing). During this time, a latex particle escapes from the focal region of microobjective O1 due to diffusion, i.e. it becomes in fact unobservable. Thus, only latex particles adhesive either to the bottom or the cover glass of a cell can be distinguished. This, probably, explains a large scatter in the measurement n_I for latex. For this reason, the concentration dependence for the latex suspension was not studied in the experiment on measurements of the scattering matrix elements.

The scattering matrix elements were measured with a modulation laser polarimeter, in which the goniometric scheme for recording scattered radiation was used (Fig. 9). The experimental setup includes a cw 532-nm laser, a lithium niobate electrooptical modulator (EOM) with the major axes oriented at an angle $\gamma = +45^\circ$ to the observation plane, two quarter-wave plates [$\lambda/4(1)$ and $\lambda/4(2)$], linear polariser P1 and linear polariser-analyser P2. An important element of the setup is a semi-cylindrical Pyrex cell of radius $R = 6$ cm, which, after filling with liquid under study, is transformed to a collecting cylindrical lens amplifying a weak scattered signal. The focal distance of this lens is $f = R_c n(n-1)^{-1} = 24$ cm, where $n = 1.33$ is the refractive index of water. The focal distance of the cell filled with liquid was determined experimentally, and these measurements were confirmed by the estimate by the expression presented above. The setup contained iris (A1), circular (A2), and slit (A3) apertures, a photomultiplier (PMT), and a low-frequency master oscillator (MO) producing the control signal at the electrodes of the modulator at the frequency $\omega/2\pi = 1.7$ kHz. An optical pair (OP) with chopper (C) was necessary for the synchronous detection of the scattered radiation intensity. The results of measurements were processed with a PC connected with an analog-to-digital converter (ADC). Iris aperture A1 was mounted directly in front of the cell and minimised the contribution of radiation scattered from optical elements located in front of the cell to the useful signal. Circular aperture A2 was mounted directly behind the cell and was used for two purposes. First, the special design of this aperture minimised the contribution of parasitic flashes to the useful signal and, second, the aperture 'cut out' at a fixed scattering angle θ a segment of length $d/\sin\theta$ (where $d = 8$ mm is the aperture diameter) from an extended source of scattered radiation, which was the laser beam track in the cell. This reduced aberrations of the cell lens with liquid under study. Slit aperture A3 was mounted in the focus of the lens, formed by the cell with liquid, directly in front of the photomultiplier cathode. The photomultiplier with aperture A3 and some polarisation elements (which were varied depending on the matrix element being measured) were mounted on a movable rail of the goniometer, which was declined from the optical axis by the scattering angle θ during measurements. The optical axis itself was specified by the incident laser beam. Thus, only the beams that were scattered and focused by the cell lens at the certain angle θ fell on the photomultiplier cathode.

Note that we took special efforts to minimise scattering at the input and output windows of the cell by their polishing, degreasing and removal of dust from them. The goniometer was calibrated by angles in the following way. Before measurements, the movable rail of the goniometer was oriented along the laser beam to obtain the maximum output signal of the photomultiplier. This orientation of the rail corresponded to the reading of the goniometer scale $\theta = 0$, i.e. to the direction along the optical axis. Scattering angles were measured from this position.

Consider the operation principle of the polarimeter. The laser radiation passes through polariser P1, which specifies the initial Stokes vector

$$\boldsymbol{S}_0 = I_0(\,1 \quad 1 \quad 0 \quad 0\,)^{\mathbf{T}},$$

where I_0 is the input laser radiation intensity. The transformation of the initial Stokes vector $\boldsymbol{S}_0$ by the

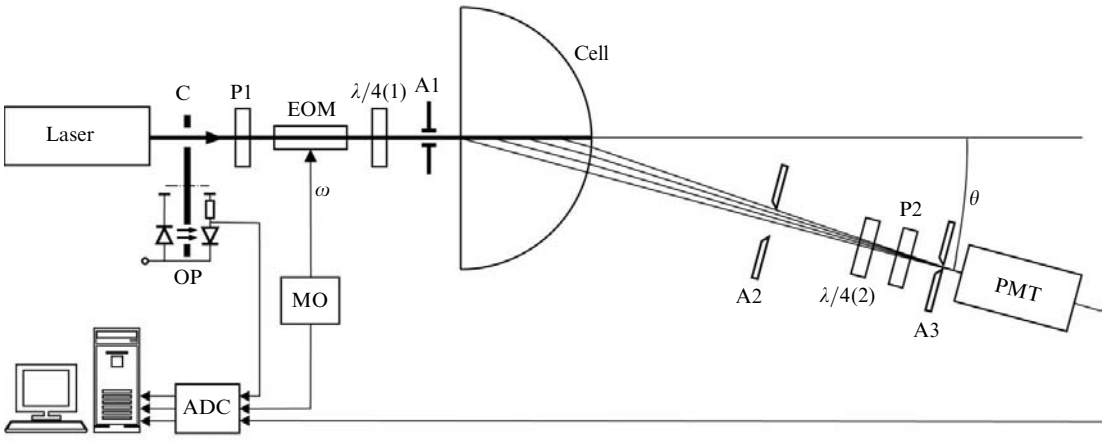

Figure 9. Scheme of a modulation laser polarimeter.

total optical system represents the successive multiplication of this vector by the Mueller matrices of the corresponding elements of the optical scheme. The Stokes vector of radiation propagated through the optical system is

$$\boldsymbol{S} = (\boldsymbol{P}_2 \cdot \boldsymbol{Q}_3 \cdot \boldsymbol{F} \cdot \boldsymbol{Q}_1 \cdot \boldsymbol{M})\boldsymbol{S}_0, \tag{9}$$

where $\boldsymbol{F}$ is the Mueller matrix of the cell with liquid under study, which has the general form

$$\boldsymbol{F} = \begin{pmatrix} F_{11} & F_{12} & F_{13} & F_{14} \\ F_{21} & F_{22} & F_{23} & F_{24} \\ F_{31} & F_{32} & F_{33} & F_{34} \\ F_{41} & F_{42} & F_{43} & F_{44} \end{pmatrix}.$$

The matrices of the modulator $\boldsymbol{M}(\delta)$, polariser $\boldsymbol{P}_2(\alpha)$, and quarter-wave plates $\boldsymbol{Q}_i = \boldsymbol{Q}(\psi_i)$ with axes making angles α и ψ_i $(i = 1, 2)$ with the plane of observation are known and have the form [24]

$$\boldsymbol{P}_2(\alpha) = \frac{1}{2}\begin{pmatrix} 1 & \cos 2\alpha & \sin 2\alpha & 0 \\ \cos 2\alpha & \cos^2 2\alpha & \sin 2\alpha \cos 2\alpha & 0 \\ \sin 2\alpha & \sin 2\alpha \cos 2\alpha & \sin^2 2\alpha & 0 \\ 0 & 0 & 0 & 0 \end{pmatrix},$$

$$\boldsymbol{M}(\delta) = \begin{pmatrix} 1 & 0 & 0 & 0 \\ 0 & \cos\delta & 0 & -\sin\delta \\ 0 & 0 & 1 & 0 \\ 0 & \sin\delta & 0 & \cos\delta \end{pmatrix},$$

$$\boldsymbol{Q}(\psi_i) = \begin{pmatrix} 1 & 0 & 0 & 0 \\ 0 & \cos^2 2\psi_i & \cos 2\psi_i \sin 2\psi_i & -\sin 2\psi_i \\ 0 & \cos 2\psi_i \sin 2\psi_i & \sin^2 2\psi_i & \cos 2\psi_i \\ 0 & \sin 2\psi_i & -\cos 2\psi_i & 0 \end{pmatrix}.$$

Here, δ is the phase shift introduced by the modulator. The intensity I detected with a photodetector corresponds to the first component of the vector $\boldsymbol{S}$. By performing multiplication in (9), we obtain

$$I = \frac{1}{2} I_0(A_0 + A_\mathrm{s} \sin\delta + A_\mathrm{c} \cos\delta). \tag{10}$$

The coefficients A_0, A_s, and A_c in the configurations of the experimental scheme in Fig. 9 required for determining the Mueller matrix elements are presented in Table 1. These coefficients corresponds to the sets of fixed azimuthal positions of the polariser and quarter-wave plates ψ_1, ψ_2, α.

One can see from Table 1 that matrix elements can be expressed in terms of half-sums and half-differences $A_0(\psi_1, \psi_2, \alpha)$, $A_\mathrm{s}(\psi_1, \psi_2, \alpha)$, and $A_\mathrm{c}(\psi_1, \psi_2, \alpha)$.

In the case of the harmonic modulation $\delta = \delta_0 \cos\omega t$, the functions $\cos\delta$ and $\sin\delta$ in expression (10) can be expanded in a Bessel series

Table 1.

ψ_1/deg	ψ_2/deg	α/deg	A_0	A_s	A_c
0	0	0	$F_{11} + F_{21}$	$F_{13} + F_{23}$	$F_{12} + F_{22}$
0	0	90	$F_{11} - F_{21}$	$F_{13} - F_{23}$	$F_{12} - F_{22}$
0	0	±45	$F_{11} \pm F_{41}$	$F_{13} \pm F_{43}$	$F_{12} \pm F_{42}$
0	45	±45	$F_{11} \pm F_{31}$	$F_{13} \pm F_{33}$	$F_{12} \pm F_{32}$
45	0	0	$F_{11} + F_{21}$	$-(F_{12} + F_{22})$	$F_{14} + F_{24}$
45	0	90	$F_{11} - F_{21}$	$-(F_{12} - F_{22})$	$F_{14} - F_{24}$
45	0	±45	$F_{11} \pm F_{41}$	$-(F_{12} \pm F_{42})$	$F_{14} \pm F_{44}$
45	45	±45	$F_{11} \pm F_{31}$	$-(F_{12} \pm F_{32})$	$F_{14} \pm F_{34}$

$$\cos\delta = J_0(\delta_0) + 2\sum_{n=1}^{\infty}(-1)^n J_{2n}(\delta_0)\cos(2n\omega t) = J_0(\delta_0) - 2J_2(\delta_0)\cos(2\omega t) + 2J_4(\delta_0)\cos(4\omega t) - \ldots, \tag{11}$$

$$\sin\delta = 2\sum_{n=0}^{\infty}(-1)^n J_{2n+1}(\delta_0)\cos[(2n+1)\omega t] = 2J_1(\delta_0)\cos(\omega t) - 2J_3(\delta_0)\cos(3\omega t) + \ldots. \tag{12}$$

If the modulation amplitude is chosen such that $J_0(\delta_0) = 0$, i.e. $\delta_0 = 2.404$ rad, the constant component of the detected signal will be proportional only to the coefficient A_0. Thus, the radiation intensity will be described by the Fourier series in cosines

$$I(t) = I_0\left[\frac{a_0}{2} + \sum_{n=1}^{\infty} a_{n\omega}\cos(n\omega t)\right]. \tag{13}$$

It follows from (13) that

$$A_0 = a_0, \;\; A_\mathrm{s} = a_\omega / J_1(\delta_0), \;\; A_\mathrm{c} = a_{2\omega}/J_2(\delta_0).$$

Thus, all the 16 elements of the Mueller matrix can be readily obtained by measuring coefficients a_0, a_ω, and $a_{2\omega}$ of the Fourier series, which are automatically detected for each of the configurations of the optical scheme presented in Table 1 by the method of lock-in detection digitally realised by a PC equipped with the ADC.

3.3 Discussion of the results

Figure 10 presents the results of measurements of the Mueller matrix elements

$$F_{11}^{(\mathrm{w})}(\theta), \quad -f_{12}^{(\mathrm{w})}(\theta) = -\frac{F_{12}^{(\mathrm{w})}(\theta)}{F_{11}^{(\mathrm{w})}(\theta)}, \quad f_{22}^{(\mathrm{w})}(\theta) = \frac{F_{22}^{(\mathrm{w})}(\theta)}{F_{11}^{(\mathrm{w})}(\theta)},$$

$$f_{33}^{(\mathrm{w})}(\theta) = \frac{F_{33}^{(\mathrm{w})}(\theta)}{F_{11}^{(\mathrm{w})}(\theta)}, \quad f_{34}^{(\mathrm{w})}(\theta) = \frac{F_{34}^{(\mathrm{w})}(\theta)}{F_{11}^{(\mathrm{w})}(\theta)}, \quad f_{44}^{(\mathrm{w})}(\theta) = \frac{F_{44}^{(\mathrm{w})}(\theta)}{F_{11}^{(\mathrm{w})}(\theta)}$$

for twice distilled water purified from solid impurities (the superscript 'w' refers to a cell with water). The rest of the matrix elements (normalised) did not exceed 0.05. Thus, we can assume that the Mueller matrix has the block-diagonal structure. Figure 10 also presents experimental data for an empty cell (the corresponding matrix elements are denoted by the subscript 'e') and the results of theoretical calculations of the Mueller matrix elements normalised to their values for $\theta = 0$ for air spheres distributed by the logarithmically normal law with parameters $r_\mathrm{eff} = 100$ nm, $v_\mathrm{eff} = 0.01$; $r_\mathrm{eff} = 500$ nm, $v_\mathrm{eff} = 0.01$; $r_\mathrm{eff} = 1$ μm, $v_\mathrm{eff} = 0.15$; and $r_\mathrm{eff} = 1.5$ μm, $v_\mathrm{eff} = 0.025$. These dependences were obtained by using program codes based of the T-matrix method [2]. Note that in this case the choice of air spheres with $r_\mathrm{eff} = 0.5$ μm and $v_\mathrm{eff} = 0.1$ is related to the results obtained with the help of an interference modulation microscope for water purified from impurities (see Fig. 7a). Figure 10 also presents the angular dependences of the Rayleigh matrix elements [see expression (7)] describing by particles of size considerably smaller than the wavelength. Hereafter, the experimental points were obtained by averaging over ten measurements. The root-mean-square deviation of experimental points for normalised matrix elements did not exceed 5×10^{-2}; this error is not indicated in the dependences presented in figures.

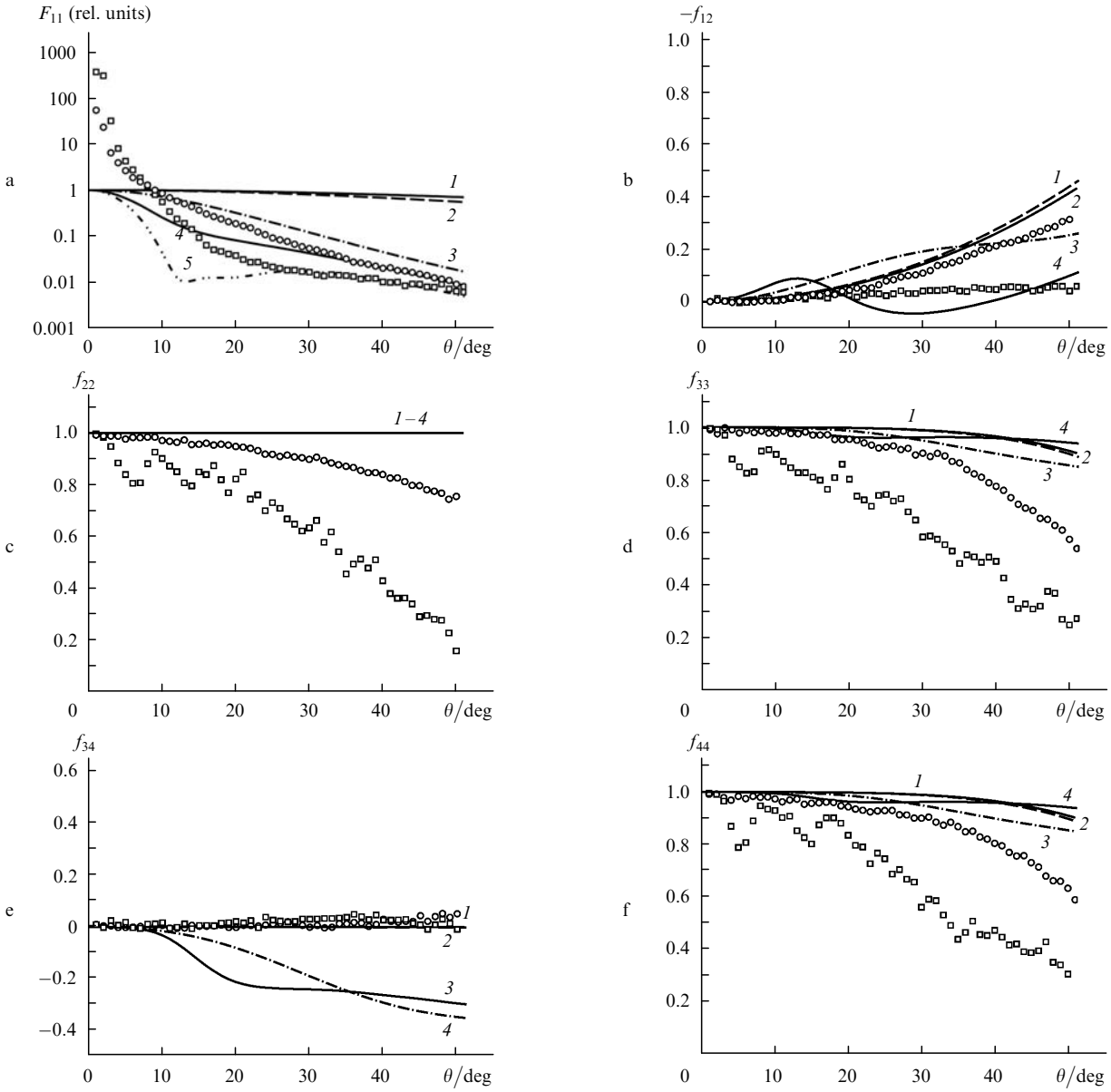

Figure 10. Light scattering matrix elements for highly purified water as functions of the scattering angle θ. Experimental data: filled cell (circles); empty cell (squares). Theoretical dependences for Rayleigh particles [see (7)] (*1*) and for air spheres with the following parameters of the logarithmically normal distribution: $r_{\text{eff}} = 100$ nm, $v_{\text{eff}} = 0.01$ (*2*); $r_{\text{eff}} = 500$ nm, $v_{\text{eff}} = 0.01$ (*3*), $r_{\text{eff}} = 1$ μm, $v_{\text{eff}} = 0.1$ (*4*); and $r_{\text{eff}} = 1.5$ μm, $v_{\text{eff}} = 0.025$ (*5*).

Figure 10a shows the experimental dependences $F_{11}^{(\text{w})}(\theta)$ and $F_{11}^{(\text{e})}(\theta)$. It follows from the form of the function $F_{11}^{(\text{e})}(\theta)$ that a considerable contribution to the scattering indicatrix of purified water in the angular range $0 < \theta < 10^\circ$ is introduced by the cell*. One can see that for angles $0 \leqslant \theta \leqslant 5^\circ$, the function $F_{11}^{(\text{e})}(\theta)$ is greater than $F_{11}^{(\text{w})}(\theta)$, which is, probably, explained by extinction in water. In the angular range $25^\circ \leqslant \theta \leqslant 50^\circ$, the element $F_{11}^{(\text{e})}(\theta)$ has asymptotics close to the Rayleigh one. At the same time, the element $F_{11}^{(\text{w})}(\theta)$ cannot be approximated by the scattering indicatrix for Rayleigh particles in the entire range of scattering angles. It follows from Fig. 10 that for scattering angles $\theta > 10$, i.e. when the influence of the cell can be neglected, the dependence $F_{11}^{(\text{w})}(\theta)$ also cannot be approximated by theoretical dependences for air spheres (Mie particles) with the fixed parameters of the logarithmically normal distribution. Obviously, we are dealing here with the air Mie sphere in a pure form. We will show below that the dependence $F_{11}^{(\text{w})}(\theta)$ obtained in our experiments can be related to the scattering of radiation by an ensemble of clusters consisting of polydisperse spherical monomers – gas nanobubbles.

Figure 10b presents the angular dependences of the matrix elements $-f_{12}^{(\text{w})}(\theta)$ and $-f_{12}^{(\text{e})}(\theta)$. One can see that the element $-f_{12}^{(\text{e})}(\theta)$ is zero in the entire angular range studied. Here, as in Fig. 10a, curve (*4*) presents the result of calculations of scattering by air Mie spheres with the parameters of the logarithmically normal distribution $r_{\text{eff}} = 1$ μm and $v_{\text{eff}} = 0.1$. Obviously, this dependence is unsuitable for the approximation of the function $-f_{12}^{(\text{w})}(\theta)$. At the same time, the dependence $-f_{12}^{(\text{w})}(\theta)$ can be approximated by a theoretical curve for Rayleigh air spheres (at least, in the angular range $0 < \theta < 40^\circ$). Thus, it follows

* Note that the scattering of light at small angles in this experiment occurs both in the cell and elements of the optical scheme.

from the curves in Figs 10a, b that micron air spheres, whose presence is confirmed in experiments with a modulation interference microscope, are, probably, not monolithic and consist of individual Rayleigh monomers (gas nanospheres). Note that dependences of this type are typical for nanoparticle clusters [9, 10]. Namely, the dependence $F_{11}^{(w)}(\theta)$ neither corresponds to spherical Mie particles nor Rayleigh particles, whereas the matrix element $-f_{12}^{(w)}(\theta)$ (at least, in the angular range $0 < \theta < 40^\circ$) behaves as if scattering occurred by monomers composing a cluster; in this case, monomers should be close to Rayleigh particles.

Figure 10c presents the dependences $f_{22}^{(w)}(\theta)$ and $f_{22}^{(e)}(\theta)$. It follows from theoretical calculations that this matrix element should be equal to unity both for Rayleigh spheres and Mie particles in the entire range of scattering angles. However, experimental dependences $f_{22}^{(w)}(\theta)$ for water considerably differ from theoretical dependences for spherical particles. This discrepancy can be caused by the deviation from the spherical shape of scatterers, which is manifested in the case of cluster aggregates. It is also caused by the influence of the cell, which is confirmed by the dependence $f_{22}^{(e)}(\theta)$.

Figures 10d, f present the angular dependences $f_{33}^{(w)}(\theta)$, $f_{33}^{(e)}(\theta)$ and $f_{44}^{(w)}(\theta)$, $f_{44}^{(e)}(\theta)$. One can see that all these matrix elements behave similarly and do not correspond to theoretical calculations for Rayleigh air spheres and air Mie spheres. Note that plots for these matrix elements for an empty cell are located considerably lower than those for water.

The measured values of matrix elements $f_{34}^{(w)}(\theta)$ and $f_{34}^{(e)}(\theta)$ in Fig. 10e lie near zero; the deviation from zero does not exceed 0.05 and are, probably, related to the measurement error. Note that this dependence is predicted by theoretical simulations of scattering in clusters consisting of Rayleigh spherical monomers [9, 10].

Figure 11 presents again the experimental angular dependences of the Mueller matrix elements for water (data for an empty cell are absent) and the corresponding theoretical dependences obtained by calculating the radiation intensity scattered by clusters consisting of polydisperse spherical nanobubbles (monomers) in water. Matrix elements for clusters were calculated for logarithmically normal distributions of monomers with parameters $r_{\text{eff}} =$ 90 nm, $\upsilon_{\text{eff}} = 0.02$, $N = 100$; $r_{\text{eff}} = 80$ nm, $\upsilon_{\text{eff}} = 0.03$, $N = 140$; and $r_{\text{eff}} = 70$ nm, $\upsilon_{\text{eff}} = 0.04$, and $N = 210$ (N is the number of monomers in a cluster). The parameters of clusters were chosen to provide the best fit of the experimental dependence $F_{11}^{(w)}(\theta)$, and clusters themselves had approximately equal scattering cross sections C_{sca} [see (5)]. Note that we did not solve the rigorous inverse problem of determining the size of particles from scattering data, but the size was estimated by selecting the values of parameters within the framework of a quite narrow parametric model. The clusters with indicated parameters are shown in Fig. 12.

The formation of clusters was numerically simulated in the following way. Each new spherical particle with radius determined by the logarithmically normal distribution was attached with the equal probability to any point on the surface of a cluster formed at the previous step. The fractal dimensionality of the obtained clusters was calculated from the dependence of the total volume V of spheres, contained inside a sphere of radius r circumscribed around the cluster centre, on r. This dependence can be everywhere, except the more porous external envelope of the cluster, approximated by a power function with the exponent D_{f}, which is the fractal dimensionality of the cluster [24]. The algorithm for calculating D_{f} is illustrated in Fig. 13 for a cluster shown in Fig. 12c. The fractal dimensionality determined in this way for the total number of monomers $10^2 - 10^3$ is $D_{\text{f}} = 2.4-2.8$. Clusters formed by the method described above and used in our paper are similar to clusters formed in a ballistic model of the attachment of individual particles [10, 24].

The theoretical dependences presented in Fig. 11 were obtained by averaging over eleven orientations in the scattering plane obtained by the rotation of clusters around the y axis within $0-180^\circ$. We used in calculations a software developed in accordance with the mathematical model of scattering by cluster particles [11]. This program is based on the known T-matrix method (see, for example, [2]). One can see that experimental data for matrix elements can be approximated with good accuracy with the help of clusters of gas nanobubbles. It is most likely that we are dealing with different types of such clusters, and experimental dependences in Fig. 11 are the result of averaging over the entire ensemble of clusters. It also follows from these dependences that the stabilisation of nanobubbles is not necessarily related to the penetration of gas molecules into pores and microcracks of macroscopic solid particles [14, 15]. Indeed, the presence of solid macroparticles is not necessary for the interpretation of experimental data presented above, and these hypothetical solid macroparticles are in no way manifested in our experiments. Note also that strong deviations of the experimental dependences $f_{22}(\theta)$, $f_{33}(\theta)$, and $f_{44}(\theta)$ from theoretical calculations for clusters are caused exclusively by the influence of a cell. This follows from calibration experiments with polystyrene latex and colloidal silica described below (Figs 14 and 15).

Figure 14 presents the experimental and theoretical angular dependences of the Mueller matrix for the water suspension of polystyrene latex. The experimental points are connected with splines. The experimental dependences for latex are best approximated by dashed theoretical curves. This is consistent with experimental histograms obtained for these latex particles with the help of a modulation interference microscope (Fig. 7b). The differences between the theoretical and experimental dependences are, probably, related to the influence of the cell and the additive contribution of nanobubble clusters to the scattered signal. As in Fig. 11, the greatest discrepancy between theoretical and experimental results is observed for the normalised diagonal matrix elements $f_{22}(\theta)$, $f_{33}(\theta)$, and $f_{44}(\theta)$. Note the presence of weak oscillations of the dependences for matrix elements $f_{33}(\theta)$ and $f_{44}(\theta)$ in the angular range $0 < \theta < 40^\circ$; the nature of these oscillations remains not clear yet.

Figure 15 presents the experimental angular dependences of the Mueller matrix elements for the water suspension of colloidal silica at the initial concentration of particles $n_{\text{I}} \approx 2.1 \times 10^8$ cm^{-3} and after tenfold dilution down to the concentration $n_{\text{II}} = 0.1 n_{\text{I}}$. As in Fig. 14, the experimental points are connected by splines. For each matrix element, the results of numerical simulation are also presented which was performed for colloidal silica particles with parameters of the logarithmically normal distribution $r_{\text{eff}} = 0.625$ μm and $\upsilon_{\text{eff}} = 0.004$ corresponding to the data obtained with the help of the modulation interference microscope (Fig. 7c).

The dependence $F_{11}(\theta)$ for suspensions with the concentration n_{I} exhibits oscillations, which were smoothed

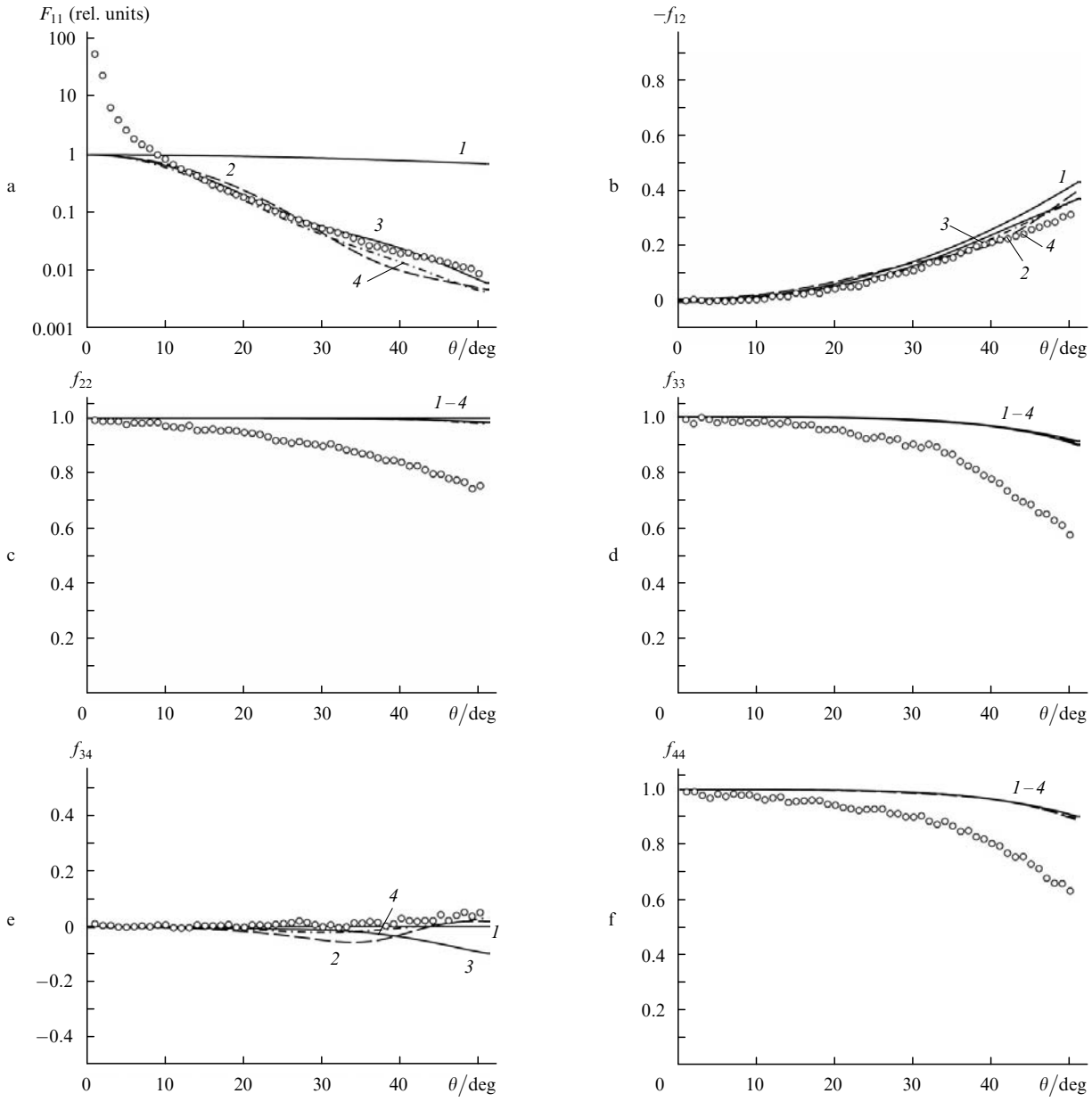

Figure 11. Light scattering matrix elements for highly purified water as functions of the scattering angle θ. Experimental data are shown by circles. Theoretical dependences are presented for Rayleigh particles [see (7)] (*1*) and clusters of polydisperse air nanospheres with the following parameters of the logarithmically normal distribution and the number of monomers: $r_{\text{eff}} = 90$ nm, $v_{\text{eff}} = 0.02$, $N = 100$ (*2*); $r_{\text{eff}} = 80$ nm, $v_{\text{eff}} = 0.03$, $N = 140$ (*3*); and $r_{\text{eff}} = 70$ nm, $v_{\text{eff}} = 0.04$, $N = 210$ (*4*).

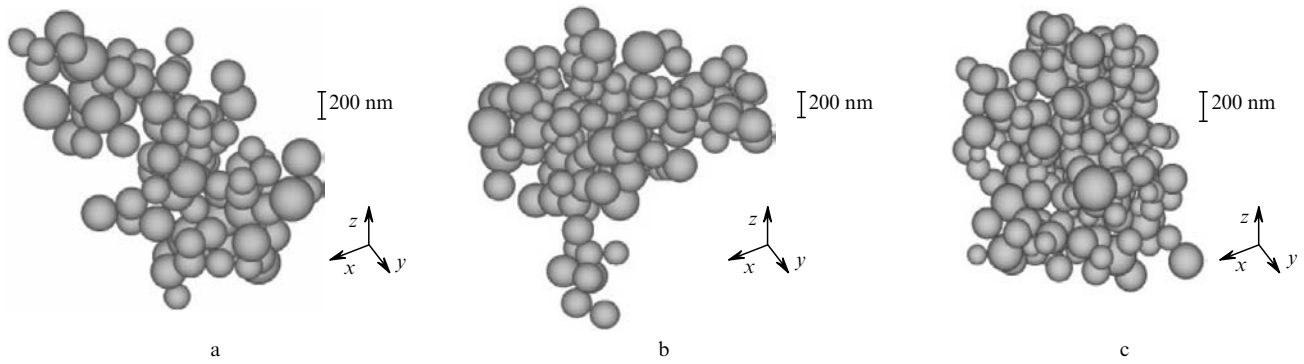

Figure 12. Models of clusters of polydisperse air nanospheres with following parameters of the logarithmically normal distribution and the number of monomers: $r_{\text{eff}} = 90$ nm, $v_{\text{eff}} = 0.02$, $N = 100$ (a); $r_{\text{eff}} = 80$ nm, $v_{\text{eff}} = 0.03$, $N = 140$ (b); and $r_{\text{eff}} = 70$ nm, $v_{\text{eff}} = 0.04$, $N = 210$ (c).

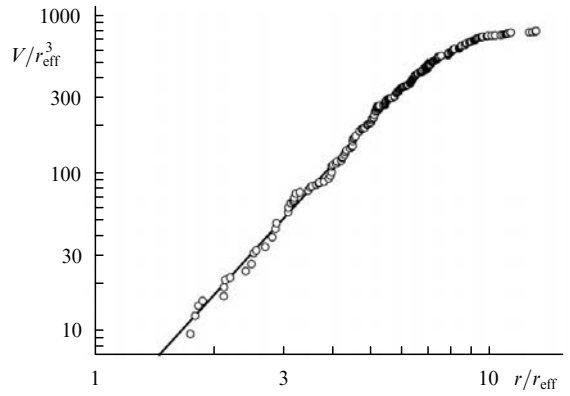

Figure 13. Dependence of the total volume V of spheres, located inside a sphere of radius r circumscribed around a cluster centre, on r for a cluster of polydisperse air nanospheres shown in Fig. 12c (○); the solid curve is the power approximation of this dependence. The fractal dimensionality of the cluster is $D_{\rm f} = 2.73$.

after the tenfold dilution of the suspension. These oscillations are caused by the diffraction of light by monodisperse spherical particles of radius $r > \lambda$ (the distribution of colloidal silica particles can be considered almost monodisperse). The type of oscillations can be easily illustrated for a strongly diluted solution of particles with the relative refractive index $n_{\rm r} \approx 1$, for which the scattering indicatrix $F_{11}(\theta)$ is described by a simple expression [25] (accurate to a dimensional factor)

$$F_{11}(\theta) \approx \langle N \rangle \Phi^2(sr), \tag{14}$$

where $s = 4\pi \sin\theta/\lambda$ is the scattering vector; $\langle N \rangle$ is the average number of particles in the scattering volume; $\Phi(sr)$ is the normalised scattering amplitude for a sphere of radius r; and $\Phi(sr) = 3(sr)^{-3}(\sin sr - sr\cos sr)$. According to (14), the dependence $F_{11}(\theta)$ for $r = r_{\rm eff} = 0.625$ μm exhibits oscillations in the angular range $0 < \theta < 90^\circ$.

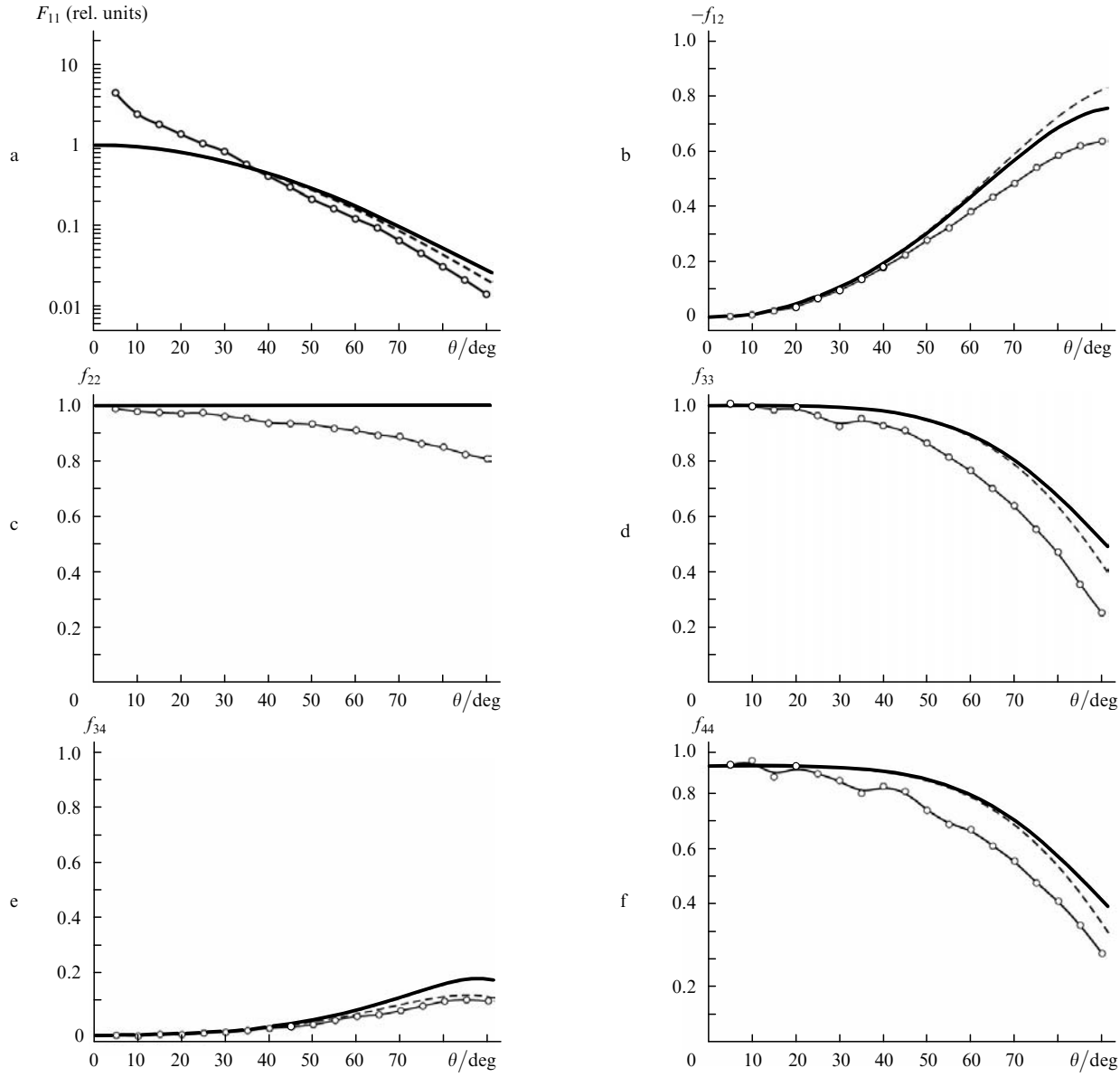

Figure 14. Light scattering matrix elements for a polystyrene latex suspension in highly purified water as functions of the scattering angle θ. Experimental data are shown by circles (thin solid curve); theoretical dependences are obtained for the following parameters of the logarithmically normal distribution: $r_{\rm eff} = 195$ nm, $v_{\rm eff} = 0.015$ (dashed curve) and $r_{\rm eff} = 185$ nm, $v_{\rm eff} = 0.025$ (thick solid curve).

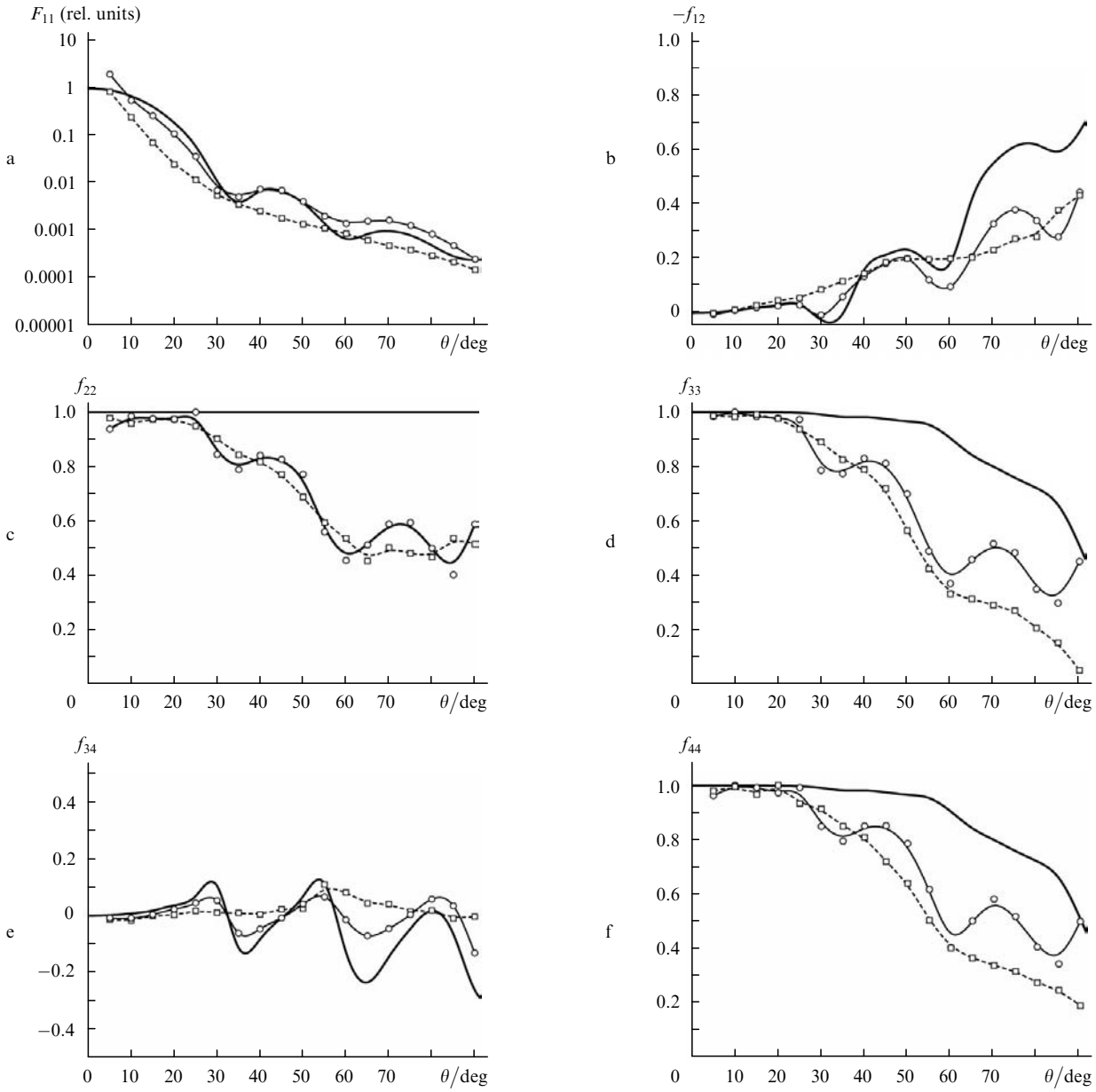

Figure 15. Light scattering matrix elements for a colloidal silica suspension in highly purified water as functions of the scattering angle θ. Experimental data are obtained at the concentrations $n_{\rm I} \approx 2.1 \times 10^8$ cm^{-3} (circles, thin solid curve) and $n_{\rm II} = 0.1 n_{\rm I}$ (squares, dashed curve); theoretical dependences are obtained for the logarithmically normal distribution with parameters $r_{\rm eff} = 0.625$ μm and $v_{\rm eff} = 0.004$ (thick solid curve).

The experimental dependences $f_{22}(\theta)$, $f_{33}(\theta)$, and $f_{44}(\theta)$ also reveal distinct characteristic oscillations. However, the theoretical angular dependences of these matrix elements show no oscillations. In our opinion, oscillations observed experimentally are caused by the combined influence of a cell and nanobubbles. Indeed, let us assume that the experimental dependence can be represented in the form

$$F_{ij}^{\rm I,II}(\theta) = \alpha C_{\rm sca}^{\rm (clust)} F_{ij}^{\rm (clust)}(\theta) + F_{ij}^{\rm (liq)}(\theta) + \beta_{\rm I,II} C_{\rm sca}^{\rm (sil)} F_{ij}^{\rm (sil)}(\theta), \quad (15)$$

where $F_{ij}^{\rm (clust)}(\theta)$ and $F_{ij}^{\rm (sil)}(\theta)$ are matrix elements for nanobubble and colloidal silica clusters, and $F_{ij}^{\rm (liq)}(\theta)$ corresponds to the matrix elements of a cell filled with liquid, but free of nanobubbles and colloidal silica particles*. The dimensional coefficients α and $\beta_{\rm I,II}$ are proportional to the concentrations of nanobubble clusters ($n^{\rm (clust)}$) and colloidal silica clusters ($n_{\rm I,II}$) in the scattering volume, respectively. Finally, $C_{\rm sca}^{\rm (clust)}$ and $C_{\rm sca}^{\rm (sil)}$ are the total scattering cross sections for nanobubble and colloidal silica clusters, which can be calculated by using software codes based on the T-matrix method and by averaging over a priori known size distribution of particles [2]. Note that the dependences $F_{ij}^{\rm (sil)}(\theta)$ and $f_{ij}^{\rm (sil)}(\theta)$ should correspond to theoretical curves, while the function $F_{11}^{\rm (sil)}(\theta)$ should oscillate according to expression (14). The smoothing of oscillations of the dependence $F_{11}^{\rm II}(\theta)$ compared to $F_{11}^{\rm I}(\theta)$ is caused by the increase in the relative contribution of non-oscillating terms in expression (15) after the tenfold decrease in the concentration.

* Note that the form of this function is unknown

Let us assume that the experimental dependences can be represented by expression (15). The experimental matrix elements $f_{ij}^{\mathrm{I,II}}(\theta)$ are obtained by normalising the function $F_{ij}^{\mathrm{I,II}}(\theta)$ to the function $F_{11}^{\mathrm{I,II}}(\theta)$, which is specified by expression (15) for $i, j = 1$ and contains both oscillating and non-oscillating terms. The latter include, obviously, $\alpha C_{\mathrm{sca}}^{(\mathrm{clust})} F_{11}^{(\mathrm{clust})}(\theta)$ and $F_{11}^{(\mathrm{liq})}(\theta)$. This means that all the normalised experimental matrix elements should exhibit oscillations with a period equal approximately to the oscillation period of the dependence $F_{11}^{\mathrm{sil}}(\theta)$. Thus, the presence of oscillations for normalised experimental matrix elements confirms the validity of representation (15).

Note that experimental results obtained for colloidal silica are especially important for the development of our model concepts. According to the theoretical model [12, 13], which is confirmed by the experimental data presented above, macroscopic scatterers in water are micron clusters consisting of air nanospheres. The calculation of the total scattering cross section for all the clusters shown in Fig. 12 by using the computer program according to the theoretical model [11] gives $C_{\mathrm{sca}}^{(\mathrm{clust})} = 0.53\ \mu\mathrm{m}^2$. Recall that scattering by clusters with such value of $C_{\mathrm{sca}}^{(\mathrm{clust})}$ provides the best fit of the experimental dependences (see Fig. 11). At the same time, for colloidal silica particles with $r_{\mathrm{eff}} = 0.625\ \mu\mathrm{m}$ and $\upsilon_{\mathrm{eff}} = 0.004$, we obtain $C_{\mathrm{sca}}^{(\mathrm{sil})} = 1.12\ \mu\mathrm{m}^2$. By using the experimental data set for pure water, we estimated unknown factors α and $\beta_{\mathrm{I,II}}$ in the angular ranges $5^\circ \leqslant \theta \leqslant 50^\circ$ and $10^\circ \leqslant \theta \leqslant 50^\circ$ by the method of least squares with the help of the algorithm

$$\alpha C_{\mathrm{sca}}^{(\mathrm{clust})} F_{11}^{(\mathrm{w})}(\theta) + \beta_{\mathrm{I,II}} C_{\mathrm{sca}}^{(\mathrm{sil})} F_{11}^{(\mathrm{sil})}(\theta) \approx F_{11}^{\mathrm{I,II}}(\theta), \qquad (16)$$

where $F_{11}^{(\mathrm{w})}(\theta)$ are experimental values of the matrix element $F_{11}(\theta)$ obtained for pure water not containing colloidal silica particles (see Figs 10a and 11a). We obtained in the angular the values $\beta_{\mathrm{I}}/\beta_{\mathrm{II}} = 9.9$, $\beta_{\mathrm{I}} C_{\mathrm{sca}}^{(\mathrm{sil})} (\alpha C_{\mathrm{sca}}^{(\mathrm{clust})})^{-1} = 188$, and $\beta_{\mathrm{I,II}} C_{\mathrm{sca}}^{(\mathrm{sil})} / \alpha C_{\mathrm{sca}}^{(\mathrm{clust})} = 19$ in the angular range $5^\circ \leqslant \theta \leqslant 50^\circ$; and $\beta_{\mathrm{I}}/\beta_{\mathrm{II}} = 10.1$, $\beta_{\mathrm{I}} C_{\mathrm{sca}}^{(\mathrm{sil})} / \alpha C_{\mathrm{sca}}^{(\mathrm{clust})} = 192$, and $\beta_{\mathrm{II}} C_{\mathrm{sca}}^{(\mathrm{sil})} / \alpha C_{\mathrm{sca}}^{(\mathrm{clust})} = 19.4$ in the angular range $10^\circ \leqslant \theta \leqslant 50^\circ$. Thus, in both cases, the ratio $\beta_{\mathrm{I}}/\beta_{\mathrm{II}}$ is close to the ratio $n_{\mathrm{I}}/n_{\mathrm{II}} = 10$, i.e. this procedure provides the measurement of relative concentrations with high enough accuracy. Note in this connection that the closeness of values of $\beta_{\mathrm{I}}/\beta_{\mathrm{II}}$ and $n_{\mathrm{I}}/n_{\mathrm{II}}$ was also verified for suspensions with different concentrations of colloidal silica particles. We neglected in (15) the term $F_{11}^{(\mathrm{liq})}(\theta)$, which seems justified in the case of a suspension of colloidal silica with concentrations $n_{\mathrm{I,II}}$ for scattering angles $\theta > 5^\circ$. If the absolute concentration $n_{\mathrm{I}} \approx 2.1 \times 10^8\ \mathrm{cm}^{-3}$ is known, the absolute concentration $n^{(\mathrm{clust})}$ of macroscopic cluster scatterers can be calculated by the expression

$$n^{(\mathrm{clust})} = \frac{\alpha}{\beta_{\mathrm{I,II}}} n_{\mathrm{I,II}} \approx 2 \times 10^6\ \mathrm{см}^{-3}.$$

This result is obtained for the angular range $10^\circ \leqslant \theta \leqslant 50^\circ$ and is averaged over the two known concentrations of the colloidal silica suspension. Thus, by adding probe particles with the known concentration and scattering cross section to liquid, we can measure the absoluter concentrations of particles in liquid. Therefore, experiments with latex and colloidal silica particles allows one not only to calibrate the experimental setup by the known test objects and substantiate the validity of the representation of the scattered signal as a sum of contributions from scattering by particles of different types, but also to estimate concentrations of these particles.

4. Conclusions

(i) Modulation interference phase microscopy experiments have shown that water purified from external solid impurities contains micron particles with the optical density lower than the optical density of water. When a layer of water evaporates, these particles also disappear. This means that they could not penetrate into water samples from outside.

(ii) Measurements of the angular dependences of the scattering matrix elements confirm that this water really contains micron particles. However, the scattering indicatrix of these particles does not correspond to that of a monolithic air sphere. This indicatrix can be best approximated by the indicatrix for an ensemble of clusters consisting of polydisperse air nanospheres.

(iii) The angular dependences of the scattering matrix elements $f_{ij}(\theta)$ are consistent with dependences for scattering by clusters with the characteristic radius $\sim 0.5\ \mu\mathrm{m}$ and the fractal dimensionality $2.4 \leqslant D_{\mathrm{f}} \leqslant 2.8$, which are formed by air nanospheres with the logarithmically normal radial distribution for $70\ \mathrm{nm} \leqslant r_{\mathrm{eff}} \leqslant 90\ \mathrm{nm}$.

(iv) In experimental studies of suspensions of colloidal particles with known concentrations and the total scattering cross section, it is possible to separate quite accurately contributions from clusters consisting of air nanospheres and calibrating colloidal particles to the total scattering indicatrix. The concentration of such clusters was estimated as $\sim 2 \times 10^6\ \mathrm{cm}^{-3}$ in our case.

Acknowledgements. This work was supported by the Russian Foundation for Basic Research (Grant Nos 06-02-16926_a, 06-02-16507_a, 08-02-90252-Uzb, 07-02-12209-ofi).

References

1. Van de Hulst H.C. *Light Scattering by Small Particles* (New York: Dover, 1981).
2. Mishchenko M.I., Travis L.D., Lacis A.A. *Scattering, Absorption, and Emission of Light by Small Particles* (Cambridge: Cambridge University Press, 2002).
3. Bohren C.F., Huffman D.R. *Absorption and Scattering of Light by Small Particles* (New York: John Wiley, 1983).
4. Hansen J.E., Travis L.D. *Space Sci. Rev.*, **16**, 527 (1974).
5. Muños O., Volten H., Hovenier J.W., Veihelmann B., van der Zande W.J., Waters L.B.F.M., Rose W.I. *J. Geophys. Res.*, **109**, D16201 (2004).
6. Kuik F., Stammes P., Hovenier J.W. *Appl. Opt.*, **30**, 4872 (1991).
7. Yang P., Wei H., Kattawar G.W., Hu Y.X., Winkler D.M., Hostetler Ch.A., Baum B.A. *Appl. Opt.*, **42**, 4389 (2003).
8. Gerrard A., Burch J.M. *Introduction to Matrix Methods in Optics* (London: John Wiley & Sons, 1975).
9. Mengüc M.P., Manickavasagam S. *Int. J. Eng. Sci.*, **36**, 1569 (1998).
10. Kimura H. *J. Quantum Spectr. & Rad. Trans.*, **70**, 581 (2001).
11. Xu Y., Wang R. *Phys. Rev. E*, **58**, 3931 (1998).
12. Bunkin N.F., Bunkin F.V. *Zh. Eksp. Teor. Fiz.*, **100**, 512 (1992).
13. Bunkin N.F., Bunkin F.V. *Zh. Eksp. Teor. Fiz.*, **123**, 828 (2003).
14. Atchley A.A., Crum L.A. *Acoustic Cavitation in Bubble Dynamics in Ultrasound: its Chemical, Physical, and Biological Effects*. Ed. by K.S. Suslick (New York: VCH Publishers, 1988) pp 1 – 64.
15. Crum L.A. *Appl. Sci. Res.*, **38**, 101 (1982).

16. Bunkin N.F., Lobeyev A.V. *Phys. Lett. A*, **229**, 327 (1997).
17. Bunkin N.F., Suyazov N.V., Tsipenyuk D.Yu. *Kvantovaya Elektron.*, **35**, 180 (2005) [*Quantum Electron.*, **35**, 180 (2005)].
18. Bunkin N.F., Ignat'ev P.S., Indukaev K.V. *Zh. Eksp. Teor. Fiz.*, **131**, 539 (2007).
19. Andreev V.A., Indukaev K.V. *J. Rus. Laser Research*, **29**, 220 (2003).
20. Iler R.K. *The Chemistry of Silica* (New York: Wiley, 1979) p. 358.
21. Hiemstra T., van Riemsdijk W.H., Bolt G.H. *J. Colloid Interface Sci.*, **133**, 91 (1989).
22. Hiemstra T., de Wit M.C., van Riemsdijk W.H. *J. Colloid Interface Sci.*, **133**, 105 (1989).
23. Behrens S.H., Borkovec M. *J. Phys. Chem.*, **103**, 2918 (1999).
24. Julien R. *Usp. Fiz. Nauk*, **157**, 339 (1989).
25. Debye P. *Z. Physik*, **28**, 135 (1927).